

# A manganese–hydrogen battery with potential for grid-scale energy storage

Wei Chen<sup>1,4</sup>, Guodong Li<sup>1,2,4</sup>, Allen Pei<sup>1</sup>, Yuzhang Li<sup>1</sup>, Lei Liao<sup>1</sup>, Hongxia Wang<sup>1</sup>, Jiayu Wan<sup>1</sup>, Zheng Liang<sup>1</sup>, Guangxu Chen<sup>1</sup>, Hao Zhang<sup>1</sup>, Jiangyan Wang<sup>1</sup> and Yi Cui<sup>1,3\*</sup>

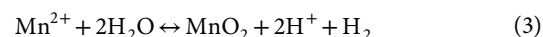
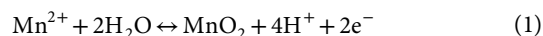
**Batteries including lithium-ion, lead–acid, redox-flow and liquid-metal batteries show promise for grid-scale storage, but they are still far from meeting the grid's storage needs such as low cost, long cycle life, reliable safety and reasonable energy density for cost and footprint reduction. Here, we report a rechargeable manganese–hydrogen battery, where the cathode is cycled between soluble Mn<sup>2+</sup> and solid MnO<sub>2</sub> with a two-electron reaction, and the anode is cycled between H<sub>2</sub> gas and H<sub>2</sub>O through well-known catalytic reactions of hydrogen evolution and oxidation. This battery chemistry exhibits a discharge voltage of -1.3 V, a rate capability of 100 mA cm<sup>-2</sup> (36 s of discharge) and a lifetime of more than 10,000 cycles without decay. We achieve a gravimetric energy density of -139 Wh kg<sup>-1</sup> (volumetric energy density of -210 Wh l<sup>-1</sup>), with the theoretical gravimetric energy density of -174 Wh kg<sup>-1</sup> (volumetric energy density of -263 Wh l<sup>-1</sup>) in a 4 M MnSO<sub>4</sub> electrolyte. The manganese–hydrogen battery involves low-cost abundant materials and has the potential to be scaled up for large-scale energy storage.**

The ever-increasing global energy consumption has driven the development of renewable energy technologies to reduce greenhouse gas emissions and air pollution<sup>1,2</sup>. Electrochemical energy storage devices, such as batteries, are critical for enabling renewable yet intermittent sources of energy such as solar and wind<sup>3,4</sup>. To date, different battery technologies have been deployed for energy storage in our everyday life<sup>5</sup>. The development of lithium-ion<sup>6,7</sup>, lead–acid<sup>8</sup>, redox-flow<sup>9–12</sup>, sodium–sulfur<sup>13</sup> and liquid-metal batteries<sup>14,15</sup> shows promise for grid-scale energy storage. However, they have various issues of low energy density (lead–acid, 30–50 Wh kg<sup>-1</sup>; redox-flow, <50 Wh l<sup>-1</sup>), poor rechargeability (lead–acid, <500 cycles; sodium–sulfur, <1,500 cycles), high cost at the battery pack level (lithium-ion, ~US\$250 kWh<sup>-1</sup>; lead–acid, ~US\$170 kWh<sup>-1</sup>; redox-flow, ~US\$450 kWh<sup>-1</sup>) and high operating temperature (sodium–sulfur, 300–350 °C; liquid-metal, >450 °C)<sup>6–15</sup>. Aqueous rechargeable batteries have significant benefits of high power output, intrinsic safety and being environmentally benign<sup>16–18</sup>. Unfortunately, limitations in the energy density and the cycle life result in a high system-level cost in US dollars per kilowatt hour. Therefore, the development of a rechargeable aqueous battery with low cost, high energy density and long cycle life is highly desirable to enable practical storage of intermittent energy sources at the grid scale.

Over the past few decades, manganese-based aqueous batteries have attracted remarkable attention due to their earth abundance, low cost, environmental friendliness and high theoretical capacity<sup>19,20</sup>. However, state-of-the-art manganese–zinc batteries show low capacity, are poorly rechargeable and suffer from dendrite formation on the zinc anode<sup>21</sup>. The rich chemistry of manganese allows it to exist in various valence states such as Mn<sup>0</sup>, Mn<sup>2+</sup>, Mn<sup>3+</sup>, Mn<sup>4+</sup> and Mn<sup>7+</sup>, providing great opportunities for the discovery of new manganese-based battery systems<sup>19</sup>.

Here, we propose and demonstrate a manganese–hydrogen (Mn–H) battery chemistry. The Mn–H battery operates by manganese deposition/dissolution reactions between soluble Mn<sup>2+</sup>

and solid MnO<sub>2</sub> at the cathode, which is fundamentally different from the solid–solid transformation in the existing Mn-based electrodes, and catalytic hydrogen evolution/oxidation reactions (HER/HOR) at the anode in soluble Mn<sup>2+</sup> solutions. The charge and discharge reactions of the Mn–H battery on the cathode (equation (1)), the anode (equation (2)) and the overall cell operation (equation (3)) can be described in the following:



## Charge storage mechanism and simulation of the Mn–H cell

As schematically depicted in Fig. 1a, our Mn–H cell is composed of a cathode-less porous carbon felt, a glass fibre separator, a Pt/C-catalyst-coated carbon felt anode and a soluble Mn<sup>2+</sup> aqueous electrolyte. MnSO<sub>4</sub> is selected as the soluble Mn<sup>2+</sup> salt due to its low cost, high solubility in water (~4.2 M at room temperature)<sup>22</sup> and the good electrochemical stability of SO<sub>4</sub><sup>2-</sup> under bias. It is worth noting that though low-cost electrocatalysts for HER/HOR such as transition-metal sulfides (MoS<sub>2</sub>), phosphides (Ni<sub>2</sub>P, CoWP) and carbides (WC) can potentially be applied to our Mn–H cell<sup>23–26</sup>, we use only Pt/C electrocatalyst in this work as a demonstration of the battery concept. When charging the Mn–H cell, soluble Mn<sup>2+</sup> ions in the electrolyte diffuse to the cathode and deposit in the form of solid MnO<sub>2</sub> on the carbon felt, while H<sub>2</sub> gas evolution from H<sub>2</sub>O is driven by highly active platinum catalysts on the anode. During discharge of the battery, the uniform layer of as-deposited MnO<sub>2</sub> on the cathode is dissolved back to soluble Mn<sup>2+</sup> electrolyte and H<sub>2</sub> is oxidized on the anode.

<sup>1</sup>Department of Materials Science and Engineering, Stanford University, Stanford, CA, USA. <sup>2</sup>Chinese Academy of Sciences (CAS) Key Laboratory of Nanosystem and Hierarchy Fabrication, CAS Center for Excellence in Nanoscience, National Center for Nanoscience and Technology, Beijing, China.

<sup>3</sup>Stanford Institute for Materials and Energy Sciences, SLAC National Accelerator Laboratory, Menlo Park, CA, USA. <sup>4</sup>These authors contributed equally: Wei Chen and Guodong Li. \*e-mail: [yicui@stanford.edu](mailto:yicui@stanford.edu)

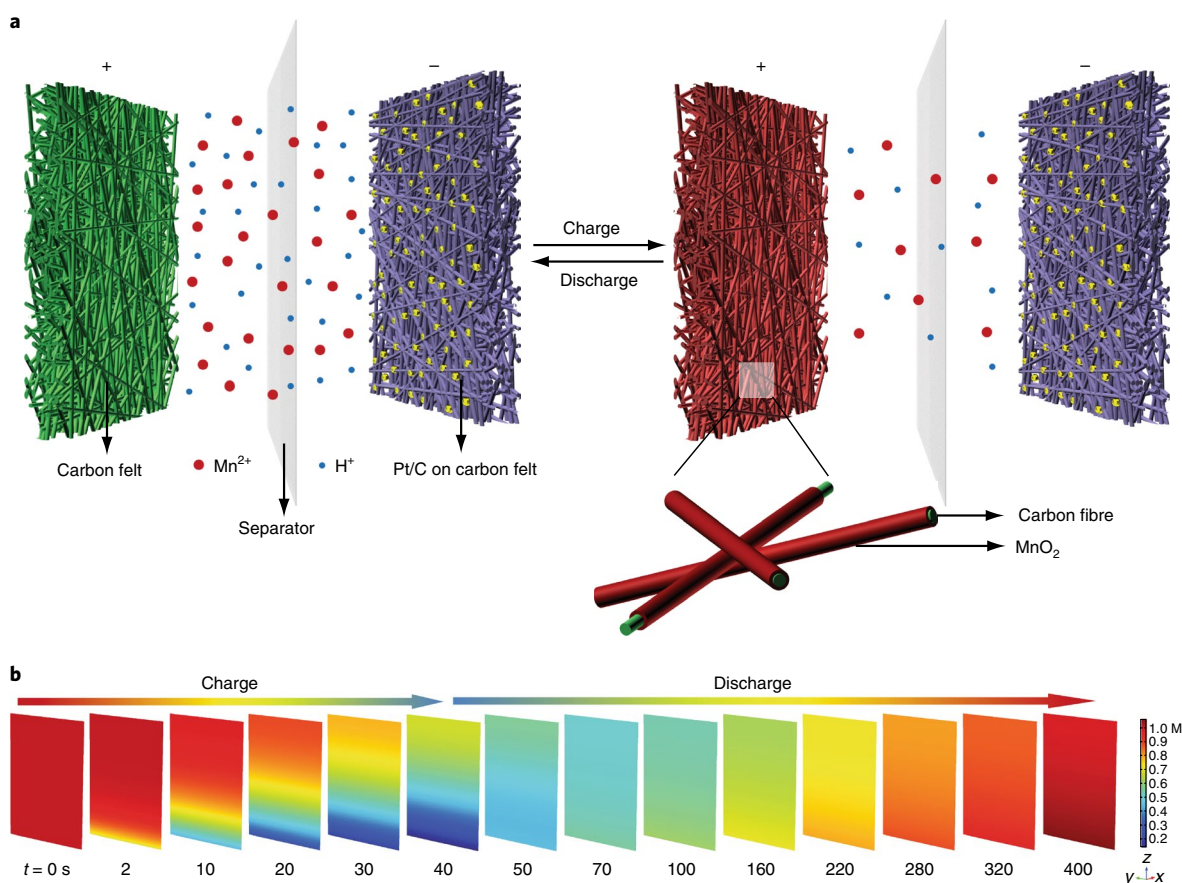


**Fig. 1 | Schematic and simulation of the Mn-H battery.** **a**, A schematic illustration of the Mn-H battery in the charge and discharge modes. Only cations ( $\text{Mn}^{2+}$  and  $\text{H}^+$ ), and not anions ( $\text{SO}_4^{2-}$ ), in the electrolyte are presented in the schematic. **b**, Representative spectra of the simulated  $\text{Mn}^{2+}$  concentration variation in the electrolyte over a complete charge and discharge process under a charge potential of 1.6 V to a capacity of  $1 \text{ mAh cm}^{-2}$  and a discharge current density of  $10 \text{ mA cm}^{-2}$ . The colour schemes show the simulated spectra of the  $\text{Mn}^{2+}$  concentration in the electrolyte at the charge and discharge process. The numbers below each spectrum indicate the charge or discharge time in seconds.

To understand the nature of the charge storage mechanism of our Mn-H cell, we applied a finite-element method in COMSOL to model the  $\text{Mn}^{2+}/\text{MnO}_2$  deposition/dissolution reactions at the cathode by simulating the dynamic electrolyte concentration variation over a complete charge and discharge process (Supplementary Fig. 1 and Supplementary Note 1). Figure 1b shows the simulated colour spectra of the electrolyte  $\text{Mn}^{2+}$  concentration in the Mn-H cell at different charge (Supplementary Fig. 2, 0–40 s) and discharge (Supplementary Fig. 3, 40–400 s) scenarios. The  $\text{Mn}^{2+}$  concentration distribution after full discharge tends to be exactly the same as that of the cell before charge (Supplementary Fig. 4), which is confirmed by the same colour spectra of the electrolyte concentration (Fig. 1b,  $t = 0$  and 400 s). The spatial variation in electrolyte concentration can be fully recovered after a complete charge and discharge cycle for the highly reversible  $\text{Mn}^{2+}/\text{MnO}_2$  deposition/dissolution reactions at fast charge rates (Supplementary Fig. 5).

### Performance of the Swagelok-type Mn-H cell

In light of the proposed and simulated energy storage mechanism, we first constructed the Mn-H cell in a custom-made Swagelok cell (Supplementary Fig. 6) and conducted the electrochemical measurements in the electrolyte of 1 M  $\text{MnSO}_4$  at room temperature. To suppress the oxygen evolution reaction (OER) on the cathode, we applied a chronoamperometric (that is, constant potential) technique with an optimal potential of 1.6 V to charge the Swagelok cell. The charge potential is lower than the measured onset potential

of  $\sim 2 \text{ V}$  for the  $\text{MnO}_2$ -coated carbon felt cathode towards obvious OER (Supplementary Figs. 7–11 and Supplementary Notes 2 and 3). The Mn-H cell was then galvanostatically (that is, constant current) discharged under different current densities. The cell in the electrolyte of 1 M  $\text{MnSO}_4$  shows a typical battery discharge behaviour with a distinct discharge plateau at  $\sim 1.2 \text{ V}$  (Supplementary Fig. 12). When charging to a capacity of  $1 \text{ mAh cm}^{-2}$ , the Coulombic efficiency of the first cycle is  $\sim 62\%$ , which then increases in subsequent cycles, reaching  $\sim 91\%$  after ten cycles (Supplementary Fig. 12). It was reported that the activity and kinetics of Pt towards HER/HOR are much higher in acid than in neutral and alkaline electrolytes<sup>27,28</sup>. With the addition of a small amount of  $\text{H}_2\text{SO}_4$  (0.05 M) into the 1 M  $\text{MnSO}_4$  electrolyte, the charge and discharge characteristics were improved drastically. The charge current of the cell in 1 M  $\text{MnSO}_4$  with 0.05 M  $\text{H}_2\text{SO}_4$  is about three times higher than that in the 1 M  $\text{MnSO}_4$  electrolyte, leading to a much shorter charge time of  $\sim 85 \text{ s}$  (Supplementary Figs. 13 and 14). In addition, the discharge plateau was increased by  $\sim 50 \text{ mV}$  (Fig. 2a), demonstrating the improved kinetics of the Mn-H cell in the electrolyte of 1 M  $\text{MnSO}_4$  with 0.05 M  $\text{H}_2\text{SO}_4$ . As such, the Coulombic efficiency of the first cycle was improved to  $\sim 70\%$ , and its discharge capacity reached  $1 \text{ mAh cm}^{-2}$  with an efficiency of 100% after the initial activation cycles (Supplementary Fig. 15). This is largely due to the synergetic effects of the higher electrolyte conductivity-induced faster  $\text{Mn}^{2+}/\text{MnO}_2$  reactions on the cathode and the more favourable HER/HOR reactions on the anode in the slightly acidic electrolyte (Supplementary Fig. 16).

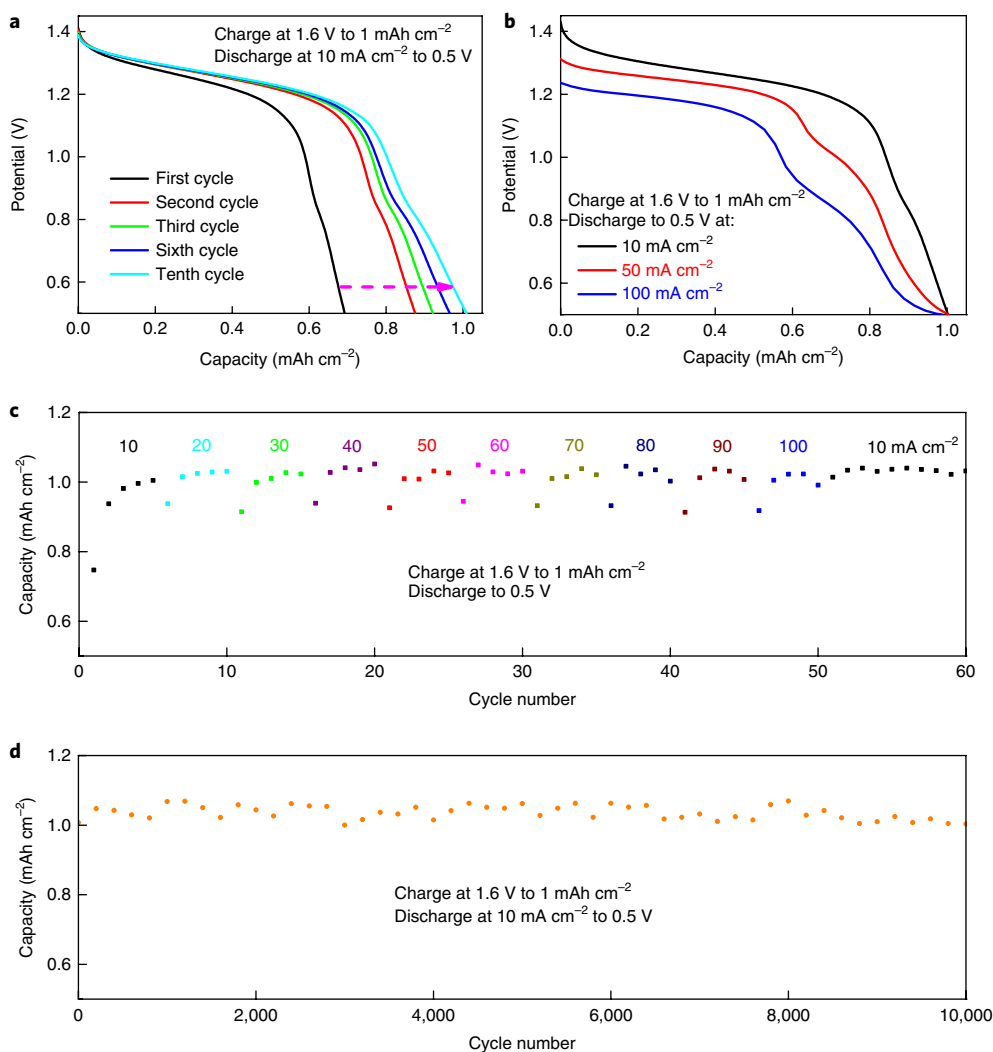


**Fig. 2 | Electrochemical performance of the Swagelok-type Mn-H cell.** **a**, The discharge behaviours of the first ten cycles in the electrolyte of 1 M MnSO<sub>4</sub> with 0.05 M H<sub>2</sub>SO<sub>4</sub>. The dashed pink arrow indicates the improved discharge performance of the Mn-H cell in the first ten cycles. **b**, The discharge curves of the cell under different current densities. **c,d**, Rate capability (**c**) and long-term stability tests (**d**) of the cell in the electrolyte of 1 M MnSO<sub>4</sub> with 0.05 M H<sub>2</sub>SO<sub>4</sub>. All cells are tested in the Swagelok-type devices at room temperature by charging at 1.6 V to 1 mAh cm<sup>-2</sup> and discharging at different current densities to 0.5 V.

The rate capability and long-term cycle stability of the batteries are of vital importance for practical energy storage applications. As shown in Fig. 2b, when the discharge current density is increased from 10 mA cm<sup>-2</sup> (discharge in 6 mins) to 50 mA cm<sup>-2</sup> and even 100 mA cm<sup>-2</sup> (discharge in 36 s), the discharge capacity of the cell can still be maintained at nearly 1 mAh cm<sup>-2</sup>. This is consistent with the capacity retention of the Mn-H cell at different rates during cycling (Fig. 2c), exhibiting a remarkable rate capability and high power density. Practically, it is demonstrated that the Mn-H cells are capable of lighting a blue light-emitting diode for a few hours when they were quickly charged at 1.6 V for only 3 min (Supplementary Fig. 17). Moreover, our Mn-H cell shows no noticeable capacity decay over 10,000 cycles at a charge capacity of 1 mAh cm<sup>-2</sup> (Fig. 2d). It is worth noting that the actual discharge capacity of the cell is slightly higher than 1 mAh cm<sup>-2</sup>. This is contributed by the extra capacity of the electrochemical double-layer capacitance of the high-surface-area carbon felt current collectors (Supplementary Fig. 18 and Supplementary Note 4). In contrast, the cell in the pure MnSO<sub>4</sub> electrolyte shows a gradual capacity decay after 400 cycles followed by severe degradation (Supplementary Fig. 19 and Supplementary Note 5), which is probably due to the

limited electrolyte conductivity and poor kinetics-induced cell failure. The energy and energy efficiency of the cell in the electrolyte of 1 M MnSO<sub>4</sub> with 0.05 M H<sub>2</sub>SO<sub>4</sub> show a similarly excellent stability to that of the discharge capacity. It is further revealed that the energy efficiency of the Mn-H cell is ~71% (Supplementary Fig. 20).

We have conducted a systematic study on the electrochemical performance of the Mn-H batteries in electrolytes of different concentrations of Mn<sup>2+</sup> with a variety of acidities. The Mn-H cells with different concentrations of Mn<sup>2+</sup>, ranging from 0.5 M to 4 M, exhibit similar electrochemical behaviours in terms of discharge potential and Coulombic efficiency (Supplementary Fig. 21). Supplementary Table 1 shows that the energy density of MnSO<sub>4</sub> electrolytes increases with concentration. However, due to the less efficient carbon felt microfibre electrode, the Mn-H cell exhibits limited electrolyte utilization (~36%) that leads to an energy density of ~19.6 Wh kg<sup>-1</sup> (based on the mass of the 1 M MnSO<sub>4</sub> + 0.05 M H<sub>2</sub>SO<sub>4</sub> + H<sub>2</sub>O electrolyte). To optimize the energy density of the Mn-H cell, we have constructed a Swagelok cell with nanostructured carbon electrode that shows electrolyte utilization of ~74.3% in 4 M MnSO<sub>4</sub>. Accordingly, the achieved gravimetric and volumetric energy densities are 139 Wh kg<sup>-1</sup> and 210.6 Wh l<sup>-1</sup>, respectively (Supplementary

Table 2, Supplementary Fig. 22 and Supplementary Note 6). In addition, it is revealed that a further increase of the electrolyte acidity (ranging from 0.05 M to 3 M of  $\text{H}_2\text{SO}_4$  in 1 M  $\text{MnSO}_4$ ) results in better electrochemical properties in terms of shorter charge time and higher discharge potential (Supplementary Fig. 23). For example, the cell in the electrolyte of 1 M  $\text{MnSO}_4$  with 3 M  $\text{H}_2\text{SO}_4$  shows a very fast charge rate of only  $\sim 36$  s to reach a capacity of  $1 \text{ mAh cm}^{-2}$  (Supplementary Fig. 13). The cell discharge plateau is located above 1.4 V, which is an enhancement of  $\sim 200$  mV as compared to the cell in the acid-free electrolyte (Supplementary Fig. 23). However, due to the harsh condition of the very acidic electrolytes and the related corrosion issues, we focus on studying the Mn–H cell in the mildly acidic electrolyte of 1 M  $\text{MnSO}_4$  with 0.05 M  $\text{H}_2\text{SO}_4$  unless otherwise specified. The electrochemical behaviours of the Mn–H cell in different electrolytes highlight the importance of electrolyte optimization for its outstanding electrochemical performance.

### Characterization of the Mn–H cell

To confirm the energy storage mechanism of the Mn–H cell, we investigated the evolution of both the cathode and the anode by different characterizations. Ex situ scanning electron microscopy (SEM) images show that, compared to the clean surface of pristine carbon felt (Supplementary Fig. 24), the carbon felt cathode after the first charge to  $1 \text{ mAh cm}^{-2}$  was completely covered with a uniform layer of  $\text{MnO}_2$  (Fig. 3a and Supplementary Fig. 25). The  $\text{MnO}_2$  was confirmed by X-ray diffraction (XRD) to be of gamma phase (Fig. 3g), which is consistent with the characteristics of electrolytic manganese dioxide<sup>29</sup>. The energy-dispersive X-ray spectroscopy (EDX) of the  $\text{MnO}_2$  shows pronounced peaks of Mn and O, further confirming the composition of  $\text{MnO}_2$  (Supplementary Fig. 25). High-resolution SEM reveals a nanoporous layer of  $\text{MnO}_2$  with nearly vertically aligned nanosheets (Fig. 3b), which were further characterized by transmission electron microscopy (TEM) to be of a crumpled and entangled nanostructure (Fig. 3c and Supplementary Fig. 26). High-resolution TEM shows the lattice fringes of 0.24 nm and 0.26 nm, corresponding to the (131) and (031) planes of gamma  $\text{MnO}_2$ , respectively (Supplementary Fig. 27). We have carefully examined many different areas of the cathode after the first charge and confirmed the uniform deposition of  $\text{MnO}_2$  over the whole carbon felt cathode (Supplementary Fig. 28). The  $\text{MnO}_2$  on the cathode disappeared after the first full discharge to 0.5 V, returning the carbon felt back to its pristine morphology (Fig. 3d and Supplementary Fig. 29). This is in good agreement with the XRD results, showing the disappearance of the characteristic peaks of  $\text{MnO}_2$  (Fig. 3g). Observation of different areas over the whole cathode confirmed the thorough dissolution of the  $\text{MnO}_2$  following full discharge, and EDX shows only carbon peaks on the cathode (Supplementary Fig. 29). However, it was found that a small amount of the  $\text{MnO}_2$  residue remained on the carbon fibre, probably due to the incomplete dissolution of  $\text{MnO}_2$  in the first discharge process (Fig. 3e). The  $\text{MnO}_2$  residues were characterized by TEM to be of a similar morphology to the deposited  $\text{MnO}_2$  (Fig. 3f and Supplementary Fig. 30). In addition, numerous nanopores are clearly visible on the discharged  $\text{MnO}_2$  residues (Fig. 3f), which were formed by the gradual dissolution of the  $\text{MnO}_2$  during discharge and were left as traces of the incomplete dissolution. To better understand the charge storage mechanism of the Mn–H cell, we investigated the cathode under different discharge cutoff voltages and over long-term cycles. For example, when the cell was not fully discharged (cutoff voltage of  $\sim 1.2$  V), the cathode shows the morphology of a partially coated carbon fibre with  $\text{MnO}_2$ , demonstrating that the discharge process is indeed a gradual dissolution process (Supplementary Fig. 31). The XRD of the cathode discharged to 1.2 V shows much weaker crystalline peaks of  $\text{MnO}_2$  as compared to its charged state (Supplementary Fig. 31). In particular, the cathode of the Mn–H cell after the long-term 10,000 cycles still shows the well-maintained morphology of

the carbon fibre without  $\text{MnO}_2$  deposits, which is confirmed by the EDX and XRD spectra (Supplementary Fig. 32).

To evaluate the oxidation state of the deposited  $\text{MnO}_2$ , we have performed X-ray photoelectron spectroscopy (XPS) measurements on the cathode under the charged and discharged stages. The cathode after charging to  $1 \text{ mAh cm}^{-2}$  shows pronounced Mn spectra, which completely disappeared when fully discharged (Supplementary Fig. 33). The core-level spectra of Mn 3s and O 1s were utilized to determine the manganese oxidation states as suggested previously<sup>30,31</sup>. In the case of the cathode at its charged state, the average oxidation state of  $\text{MnO}_2$  was calculated to be 3.9 on the basis of the Mn 3s peak splitting energy of 4.47 eV (Fig. 3h)<sup>31</sup>. Therefore, the actual electron charge transfer number in the Mn–H cell is 1.9. In addition, the deconvoluted O 1s spectrum can be fitted with three components that are associated with the Mn–O–Mn bond (529.7 eV) for tetravalent  $\text{MnO}_2$ , the Mn–OH bond (531.2 eV) for trivalent  $\text{MnOOH}$  and the H–O–H bond (532.6 eV) for residual water in the materials, respectively (Fig. 3i).

The electrochemical performance of the Mn–H cell is partially ascribed to the highly active anode towards HER/HOR. The Pt/C-coated carbon felt anode shows high HER/HOR activities with little overpotential and negligible degradation in the  $\text{H}_2$ -saturated 0.05 M  $\text{H}_2\text{SO}_4$  electrolyte (Supplementary Fig. 34). Notably, the Pt/C-carbon felt retained the same morphology and composition after the Mn–H cell tests (Supplementary Figs. 35 and 36), demonstrating its capability as the anode for both HER/HOR.

### Scale-up of the Mn–H cell

To increase the cell capacity for large-scale energy storage applications, we have developed two different approaches to scale up the energy storage capacity of the Mn–H cell. In the first approach, we have increased the cell capacity by using thicker cathode carbon felts with a larger surface area. The corresponding cells with different carbon felt cathodes are denoted as Swagelok cell I (thickness: 3.18 mm; area:  $1 \text{ cm}^2$ ), cell II (thickness: 6.35 mm; area:  $1 \text{ cm}^2$ ) and cell III (thickness: 6.35 mm; area:  $2.5 \text{ cm}^2$ ), respectively. As shown in Supplementary Fig. 37 and summarized in Fig. 4a, the discharge capacity of cell II (3.78 mAh) is nearly double that of cell I (1.9 mAh) by simply replacing the cathode with one of double thickness. Similarly, the capacity of cell III can be further increased to 8.97 mAh by increasing the cathode area by 2.5 times. The rechargeability test of cell II under a charge capacity of  $4 \text{ mAh cm}^{-2}$  shows a discharge capacity of  $3.86 \text{ mAh cm}^{-2}$  after 600 cycles (Fig. 4b), which corresponds to a capacity retention of 96.5%. However, the Mn–H cell shows capacity decay under high charge capacities (Supplementary Figs. 38–40 and Supplementary Note 7).

In the second approach towards the scale-up of the Mn–H cell, we have built a membrane-free cylindrical-type cell for large-scale energy storage. The cylindrical Mn–H cell is composed of a large piece of carbon felt, electrolyte and a small piece of Pt/C-coated carbon felt anode (Fig. 4c and Supplementary Fig. 41). A steel vessel was utilized to encapsulate all components and keep them in a hydrogen atmosphere. Owing to the unique charge storage mechanism, it is possible to utilize non-corresponding sizes of cathode and anode, providing an economic pathway to the fabrication of catalysis-based batteries by reducing the amount of catalyst at the anode. Figure 4d shows the electrochemical discharge behaviour of the cylindrical cell in the electrolyte of 1 M  $\text{MnSO}_4$  with 0.05 M  $\text{H}_2\text{SO}_4$ . Due to the same charge storage mechanism, the cylindrical cell exhibits similar electrochemical behaviours to that of the Swagelok cell (Supplementary Fig. 42). In terms of the charging rate, it takes about half an hour to reach a capacity of 15 mAh (Supplementary Fig. 43). We further observed a discharge plateau of  $\sim 1.2$  V for various charge capacities in the cylindrical cell, which is slightly lower than that of the Swagelok cell. The cylindrical cell is capable of achieving capacities of 10–20 mAh. Specifically, the first cycle discharge capacities of

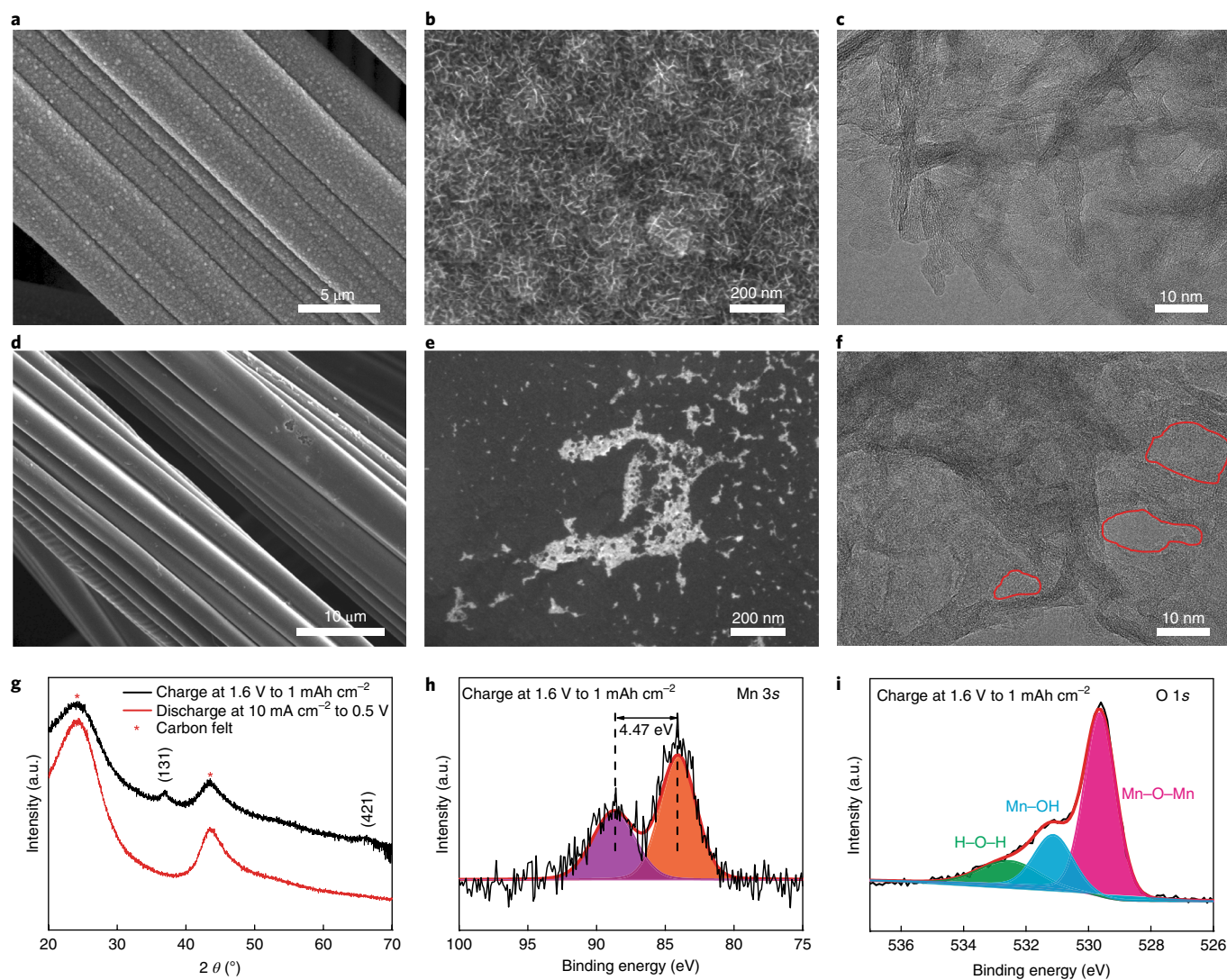


**Fig. 3 | Characterization of the cathode in the Mn-H cell. a-c,** SEM (a,b) and TEM (c) images of the cathode after the first charge at 1.6 V to 1 mAh cm<sup>-2</sup>. **d-f,** SEM (d,e) and TEM (f) images of the cathode after the first discharge at 10 mA cm<sup>-2</sup> to 0.5 V. The red circled areas in **f** indicate the generated nanopores by MnO<sub>2</sub> dissolution. **g,** XRD of the cathode after the first charge and discharge. **h,i,** XPS of Mn 3s (**h**) and O 1s (**i**) of the cathode after the first charge at 1.6 V to 1 mAh cm<sup>-2</sup>. The value of 4.47 eV in **h** refers to the Mn 3s peak splitting energy of the MnO<sub>2</sub> on the cathode. The black and red curves in **h** and **i** correspond to the experimental and fitted results of the spectra of Mn 3s and O 1s, respectively. The orange and purple spectra in **h** represent the two fitted components of the Mn 3s peak. The red, blue and green spectra in **i** represent the fitted components of the Mn-O-Mn, Mn-OH and H-O-H bonds of O 1s, respectively.

the cell under charge capacities of 10, 15 and 20 mAh are 9.7, 13.7 and 17.6 mAh, corresponding to initial Coulombic efficiencies of 97%, 91.3% and 88%, respectively. In addition, the efficiency of the cylindrical cell at a charge capacity of 15 mAh increases with the initial cycles, reaching ~96.7% within the first 50 cycles as revealed by the stability test (Fig. 4e). The long-term cycle stability result shows that the cylindrical cell achieves ~94.2% of the charge capacity of 15 mAh after 1,400 cycles (Fig. 4e). To further increase the energy storage, one can simply enlarge the vessel by applying larger sizes of the cathode carbon felts. The electrochemical performance of the Mn-H cylindrical cell demonstrates another important strategy towards large-scale energy storage applications.

### Opportunities and challenges of the Mn-H cell

Our Mn-H cell has some unique features and advantages over the previously reported battery systems. First, the Mn-H cell is constructed in the discharged state where the cathode consists of only the carbon substrate. Therefore, the fabrication of the Mn-H cell is

simplified by the cathode-less design, avoiding the complex preparation of the conventional MnO<sub>2</sub> cathode and thus providing a cost-effective approach for the battery manufacturing. Second, the manganese dissolution process, which is well known as the failure mechanism in conventional aqueous manganese batteries<sup>19</sup>, is now utilized for our benefit as the principal charge storage mechanism in the Mn-H cell. We discovered that the Mn<sup>2+</sup>/MnO<sub>2</sub> deposition-dissolution reaction is a highly reversible process, addressing the cathode rechargeability and stability issues. Third, the two-electron reaction of Mn<sup>2+</sup>/MnO<sub>2</sub> gives rise to a high theoretical capacity of 616 mAh g<sup>-1</sup> for the Mn-H cell based on the mass of solid MnO<sub>2</sub>, which doubles the value of most previous Mn batteries with a one-electron reaction<sup>21</sup> (308 mAh g<sup>-1</sup>). Fourth, we have adopted a highly reversible hydrogen electrode as the anode by utilizing Pt-catalysed HER/HOR reactions to overcome the poor rechargeability of the conventional anodes. Fifth, the fast kinetics of the Mn<sup>2+</sup>/MnO<sub>2</sub> reactions at the cathode and the HER/HOR at the anode contribute to the high rate capability of the Mn-H cell. Sixth, the high solubility

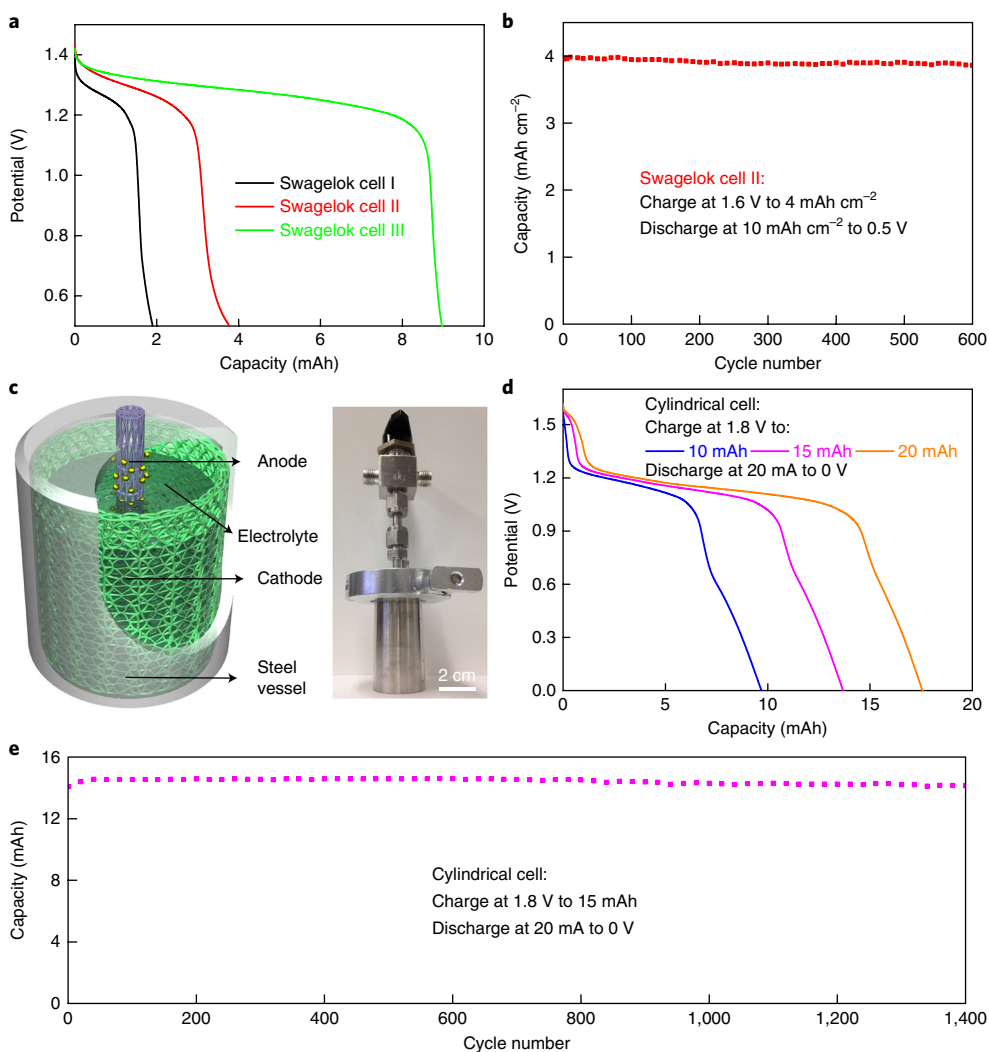


**Fig. 4 | Scale-up of the Mn-H cell.** **a**, The discharge behaviours of the Swagelok cells with three different electrode sizes. Swagelok cell I (thickness: 3.18 mm; area: 1 cm<sup>2</sup>; electrolyte volume: 100  $\mu$ l) was charged at 1.6 V to 2 mAh (2 mAh cm<sup>-2</sup>) and discharged at 10 mA cm<sup>-2</sup> to 0.5 V. Swagelok cell II (thickness: 6.35 mm; area: 1 cm<sup>2</sup>; electrolyte volume: 200  $\mu$ l) was charged at 1.6 V to 4 mAh (4 mAh cm<sup>-2</sup>) and discharged at 10 mA cm<sup>-2</sup> to 0.5 V. Swagelok cell III (thickness: 6.35 mm; area: 2.5 cm<sup>2</sup>; electrolyte volume: 500  $\mu$ l) was charged at 1.6 V to 10 mAh (4 mAh cm<sup>-2</sup>) and discharged at 10 mA cm<sup>-2</sup> to 0.5 V. **b**, The cycle stability of cell II when it was charged at 1.6 V to 4 mAh cm<sup>-2</sup> and discharged at 10 mA cm<sup>-2</sup> to 0.5 V. **c**, Schematic and digital photograph of the membrane-free cylindrical Mn-H cell. **d**, The discharge behaviour of the cylindrical cell with cathode carbon felt thickness of 6.35 mm and area of 10 cm<sup>2</sup>. The cell was charged at 1.8 V to capacities of 10, 15 and 20 mAh, and then discharged at 20 mA (2 mA cm<sup>-2</sup>) to 0 V. **e**, The cycle stability of the cylindrical cell with a charge capacity of 15 mAh. The electrolyte is 1 M MnSO<sub>4</sub> with 0.05 M H<sub>2</sub>SO<sub>4</sub>.

of the Mn<sup>2+</sup> ions in water gives rise to a high theoretical gravimetric energy density of  $\sim 174$  Wh kg<sup>-1</sup> and volumetric energy density of 263 Wh l<sup>-1</sup> in the 4 M MnSO<sub>4</sub> electrolyte (normalized to the electrolyte mass/volume including the MnSO<sub>4</sub> salt and water) for the Mn-H cell, which is substantially higher than that of the conventional Mn-based batteries. Seventh, the utilization of low-cost raw materials such as MnSO<sub>4</sub> salt, carbon felt and glass fibre separators in the Mn-H cell could make it an inexpensive system.

However, the achieved capacity and energy density of the Mn-H cell is limited by the low efficiency of the carbon felt substrate. Highly efficient substances such as carbon nanofibres are essential to the improvement of the electrochemical performance of the Mn-H cell. In addition, platinum-free electrocatalysts are needed for the development of low-cost hydrogen batteries for large-scale energy storage.

The self-discharge performance is an important consideration for battery energy storage. In terms of batteries for grid storage, 5–10 h of off-peak storage<sup>32</sup> is essential for battery usage on a daily

basis<sup>33</sup>. As shown in Supplementary Fig. 44, our Mn-H cell is capable of retaining  $\sim 95\%$  of the initial capacity after 12 h of self-discharge, indicating its practical grid storage potential. The long-term self-discharge behaviour of the Mn-H cell shows that the cell can retain a potential of  $\sim 1.254$  V after 80 h of self-discharge, although the remaining capacity is  $\sim 71\%$ . To improve the self-discharge performance of the Mn-H cell, future work could be conducted on the highly efficient cathode and anode current collectors, electrolyte purification and advanced gas management of the whole battery system (Supplementary Note 8).

## Conclusions

We reported a rechargeable battery chemistry of Mn-H with promising electrochemical performance. The Mn-H battery chemistry provides a methodology towards the development of high energy density, fast charging rates and ultrastable batteries with potentials for grid-scale energy storage. We expect further improvement of the battery performance by exploring highly efficient electrodes and

cell management systems. The cost of the Mn–H system can be further reduced by the development of highly active, earth-abundant HER/HOR electrocatalysts in the future.

## Methods

**Materials.** The chemicals and materials in this work are all commercially available and used as received: manganese sulfate monohydrate ( $\text{MnSO}_4 \cdot \text{H}_2\text{O}$ , Sigma Aldrich), sulfuric acid ( $\text{H}_2\text{SO}_4$ , Sigma Aldrich), *N*-methyl-2-pyrrolidone (NMP, Sigma Aldrich), platinum 40% on carbon (HiSPEC 4000, Fuel Cell Store), polyvinylidene fluoride (PVDF, MTI), Whatman glass fibre paper (GF 8, thickness of 350  $\mu\text{m}$ ), titanium foils (thickness of 0.127 mm and 0.5 mm, Alfa Aesar), carbon felts (thickness of 3.18 mm and 6.35 mm, Alfa Aesar) and deionized water (resistance of 18.2 M $\Omega$ , Milli Q).

**Fabrication of Swagelok and cylindrical cells.** The Swagelok cell was constructed by connecting stainless-steel inlet and outlet valves with Klein Flange (KF) to Swagelok adapters in a polytetrafluoroethylene (PTFE)-centred O-ring by a clamp (Supplementary Fig. 6). The cathode and anode were sandwiched by a glass fibre separator and assembled in a typical coin-cell stack into the Swagelok cell. A thin layer of insulating PTFE film was placed inside the aluminium clamp to isolate the cathode and anode. The cathode carbon felt was calcined at 450 °C for 2 h before acting as a current collector. The anode was prepared by pasting Pt/C slurry onto one side of the carbon felt. It was then subjected to complete drying at 60 °C under a vacuum for at least 24 h. The Pt/C slurry was prepared by mixing Pt/C powder with the PVDF binder in a weight ratio of 9:1 in NMP and stirred vigorously overnight. The Pt/C-coated side of the anode carbon felt was directly in contact with the separator in the assembly of the Swagelok cell and its other side was employed as a gas diffusion layer. High-purity Ti foils were used as conductive current collectors for the carbon felt electrodes, to avoid any possible contamination or side reactions. The assembled cell was purged with high-purity hydrogen gas (99.99%, Airgas) to remove the trapped air from the cell. The Swagelok cells were tested at room temperature under sealed conditions by locking the valves.

The cylindrical cell was built by clamping a stainless-steel cylinder with a KF to Swagelok adapter in a PTFE-centred O-ring (Supplementary Fig. 40). The stainless-steel cylinder was machined at Stanford machine shop and served as the cathode case. The cathode was constructed by rolling the calcined carbon felt into the steel cylinder. The carbon felt was then welded to the steel cylinder with Ti foil. The inner side of the steel cylinder was covered with a layer of insulating tape to avoid any contamination from the stainless-steel vessel (Supplementary Fig. 40b). The anode was built by connecting a KF to Swagelok adapter with a three-way valve. It was accomplished by welding the Pt/C-coated carbon felt with Ti foil onto the adapter (Supplementary Fig. 40c). The Pt/C-coated carbon felt was made by pasting Pt/C catalyst onto both sides of the carbon felt. In the assembled cylindrical cell, the cathode carbon felt was surrounded by the central anode with a gap of ~0.5 cm. Around 14 ml of electrolyte (1 M  $\text{MnSO}_4$  with 0.05 M  $\text{H}_2\text{SO}_4$ ) was added to the cell. The cell was then assembled and purged with high-purity hydrogen gas (99.99%, Airgas) to get rid of the trapped air. The cylindrical cells were tested at room temperature under sealed conditions by locking the valves.

**Materials characterization.** The morphology and microstructure of the electrodes were characterized by SEM (FEI XL30 Sirion) and TEM (FEI Titan). XRD was conducted by PANalytical X'Pert diffractometer using copper K-edge X-rays. XPS was performed on an SSI SProbe XPS spectrometer with an Al  $K_{\alpha}$  source. The average oxidation state of  $\text{MnO}_2$  is calculated on the basis of the following equation<sup>31</sup>:

$$\text{AOS} = 8.95 - 1.13\Delta E(\text{eV}) \quad (4)$$

where  $\Delta E$  is the energy difference between the main Mn 3s peak and its satellite peak.

**Electrochemical measurements.** The electrochemical measurements were carried out on a Biologic VMP3 multi-channel electrochemical workstation at room temperature. Due to the unique charge storage mechanism of the Mn–H cell, we applied a chronoamperometry (that is, constant potential) technique to charge our cells. Optimal potentials of 1.6 V and 1.8 V were used to charge the Swagelok cells and cylindrical cells, respectively. The cells were discharged by applying galvanostatic currents. The Swagelok and cylindrical cells were tested in a two-electrode full-cell set-up, where carbon felt was applied as the cathode substrate with Pt/C-coated carbon felt as the anode. A single layer of glass fibre separator (GF-8, Whatman, thickness of 350  $\mu\text{m}$ ) was used in the Swagelok cells, while no membrane was used in the cylindrical cells.

The OER test was conducted in a three-electrode set-up by taking  $\text{MnO}_2$ -coated carbon felt (thickness of 6.35 mm) as the working electrode, a saturated calomel electrode (SCE) as the reference electrode and a graphite rod as the counter electrode.  $\text{MnO}_2$ -coated carbon felt with a geometric area of 1  $\text{cm}^2$  was employed as the working electrode, without using any binder or conducting

additives. The electrolyte was 0.5 M  $\text{Na}_2\text{SO}_4$ . The SCE reference electrode was calibrated with respect to a reversible hydrogen electrode (RHE) in  $\text{H}_2$ -saturated 0.05 M  $\text{H}_2\text{SO}_4$  electrolyte, yielding a relation of  $E(\text{RHE}) = E(\text{SCE}) + 0.325 \text{ V}$ . Linear sweep voltammetry was performed at 0.5  $\text{mV s}^{-1}$  between 0.5 and 2 V (versus SCE). The reported current density is normalized to the geometric area of the  $\text{MnO}_2$ -coated carbon felt.

Gas chromatography measurements were performed on the 8610 C gas chromatograph (SRI Instruments) by air-tight H- and T-shaped cells (Supplementary Figs. 9 and 10 and Supplementary Notes 2 and 3).

The self-discharge measurements were conducted in the Swagelok Mn–H cell by first charging at a potential of 1.6 V to 2 mAh  $\text{cm}^{-2}$  and then relaxing for different durations. Open-circuit voltages were recorded during the relax times.

**Simulation details.** The ‘Electrodeposition, Secondary’ and ‘Transport of Diluted Species’ physics models in COMSOL were applied to simulate the reactions and concentration variations in the electrolyte. The simulation cell was rectangular with a dimension of 250  $\mu\text{m} \times 250 \mu\text{m}$  at the base and a height of 350  $\mu\text{m}$  corresponding to the separator thickness (Supplementary Fig. 1). The initial concentration of  $\text{Mn}^{2+}$  ions was set to 1 M throughout the electrolyte. The diffusion coefficient of  $\text{Mn}^{2+}$  was set to  $1.172 \times 10^{-2} \text{ cm}^2 \text{ s}^{-1}$ , estimated from an ionic conductivity of 44  $\text{mS cm}^{-1}$  using the equation of  $\sigma = n e \mu$  and the Einstein relation  $D = \mu k T$ , where  $\sigma$  is the ionic conductivity,  $\mu$  is the ion mobility,  $n$  is the ionic concentration,  $e$  is the Faraday constant to scale charge and molar concentration,  $D$  is the diffusion coefficient,  $k$  is the Boltzmann constant and  $T$  is the temperature. In the case of the charging process, the cathode was set at a constant potential of 1.6 V versus a standard hydrogen electrode. The reaction was preceded on the concentration-dependent Butler–Volmer kinetics, with an exchange current density of 8.18  $\text{A m}^{-2}$ . The charging process was terminated after a capacity of 1 mAh  $\text{cm}^{-2}$  was obtained, which was calculated to be achieved after 40 s. The cell was then subsequently discharged galvanostatically at a current density of 10 mA  $\text{cm}^{-2}$  until a capacity of 1 mAh  $\text{cm}^{-2}$  was stripped, which lasts for 360 s.

**Calculations of capacities and energy densities.** The calculations of the electrolyte utilization rate, capacities and energy densities of the Mn–H cells are normalized to the mass/volume of the electrolytes including the  $\text{MnSO}_4$  salt, additive and water. The electrolyte utilization rate is defined as the ratio of the achieved capacity over the theoretical capacity of the applied electrolyte in the Mn–H cell. The theoretical capacity is calculated on the basis of the two-electron  $\text{Mn}^{2+}/\text{MnO}_2$  reaction, which is ~1616 mAh  $\text{g}^{-1}$  with respect to the mass of solid  $\text{MnO}_2$  alone. The theoretical capacities of the electrolytes are dependent on the solubility of the  $\text{MnSO}_4$  in water, yielding a theoretical specific capacity of ~141 mAh  $\text{g}^{-1}$  and a volumetric capacity of ~214  $\text{Ah l}^{-1}$  in the 4 M  $\text{MnSO}_4$  electrolyte. The achieved specific/volumetric capacities are obtained by the actual discharge capacities (mAh) over the mass/volume of the applied electrolytes. Similarly, the theoretical energy densities of the electrolytes are dependent on the solubility of the  $\text{MnSO}_4$  in water, yielding a theoretical gravimetric energy density of ~174 Wh  $\text{kg}^{-1}$  and a volumetric energy density of ~263  $\text{Ah l}^{-1}$  in the 4 M  $\text{MnSO}_4$  electrolyte by taking the standard cell potential of 1.23 V (Supplementary Table 1). The achieved gravimetric/volumetric energy densities are obtained by the actual discharge energy (Wh) over the mass/volume of the applied electrolytes (Supplementary Table 2).

**Data availability.** The data that support the plots within this paper and other findings of this study are available from the corresponding author upon reasonable request.

Received: 12 September 2017; Accepted: 1 April 2018;

Published online: 30 April 2018

## References

1. Chu, S. & Majumdar, A. Opportunities and challenges for a sustainable energy future. *Nature* **488**, 294–303 (2012).
2. Chu, S., Cui, Y. & Liu, N. The path towards sustainable energy. *Nat. Mater.* **16**, 16–22 (2017).
3. Dunn, B., Kamath, H. & Tarascon, J. M. Electrical energy storage for the grid: a battery of choices. *Science* **334**, 928–935 (2011).
4. Rugolo, J. & Aziz, M. J. Electricity storage for intermittent renewable sources. *Energy Environ. Sci.* **5**, 7151–7160 (2012).
5. Chen, H. S. et al. Progress in electrical energy storage system: a critical review. *Prog. Nat. Sci.* **19**, 291–312 (2009).
6. Tarascon, J. M. & Armand, M. Issues and challenges facing rechargeable lithium batteries. *Nature* **414**, 359–367 (2001).
7. Goodenough, J. B. & Kim, Y. Challenges for Rechargeable Li Batteries. *Chem. Mater.* **22**, 587–603 (2010).
8. Pavlov, D. *Lead–Acid Batteries: Science and Technology: A Handbook of Lead–Acid Battery Technology and its Influence on the Product* (Elsevier, Amsterdam, 2011).
9. Wang, W. et al. Recent progress in redox flow battery research and development. *Adv. Func. Mater.* **23**, 970–986 (2013).

10. Noack, J., Roznyatovskaya, N., Herr, T. & Fischer, P. The chemistry of redox-flow batteries. *Angew. Chem. Int. Ed.* **54**, 9775–9808 (2015).
11. Huskinson, B. et al. A metal-free organic–inorganic aqueous flow battery. *Nature* **505**, 195–198 (2014).
12. Yang, Y., Zheng, G. Y. & Cui, Y. A membrane-free lithium/polysulfide semi-liquid battery for large-scale energy storage. *Energy Environ. Sci.* **6**, 1552–1558 (2013).
13. Oshima, T., Kajita, M. & Okuno, A. Development of sodium–sulfur batteries. *J. Appl. Ceram. Tech.* **1**, 269–276 (2004).
14. Wang, K. L. et al. Lithium–antimony–lead liquid metal battery for grid-level energy storage. *Nature* **514**, 348–350 (2014).
15. Kim, H. et al. Liquid metal batteries: past, present, and future. *Chem. Rev.* **113**, 2075–2099 (2013).
16. Ovshinsky, S. R., Fetcenko, M. A. & Ross, J. A nickel metal hydride battery for electric vehicles. *Science* **260**, 176–181 (1993).
17. Li, W., Dahn, J. R. & Wainwright, D. S. Rechargeable lithium batteries with aqueous electrolytes. *Science* **264**, 1115–1118 (1994).
18. Beck, F. & Ruetschi, P. Rechargeable batteries with aqueous electrolytes. *Electrochim. Acta.* **45**, 2467–2482 (2000).
19. Zhang, K. et al. Nanostructured Mn-based oxides for electrochemical energy storage and conversion. *Chem. Soc. Rev.* **44**, 699–728 (2015).
20. Wei, W. F., Cui, X. W., Chen, W. X. & Ivey, D. G. Manganese oxide-based materials as electrochemical supercapacitor electrodes. *Chem. Soc. Rev.* **40**, 1697–1721 (2011).
21. Pan, H. L. et al. Reversible aqueous zinc/manganese oxide energy storage from conversion reactions. *Nat. Energy* **1**, 16039 (2016).
22. Cottrell, F. G. On the solubility of manganous sulphate. *J. Phys. Chem.* **4**, 637–656 (1900).
23. Li, Y. G. et al. MoS<sub>2</sub> nanoparticles grown on graphene: an advanced catalyst for the hydrogen evolution reaction. *J. Am. Chem. Soc.* **133**, 7296–7299 (2011).
24. Popczun, E. J. et al. Nanostructured nickel phosphide as an electrocatalyst for the hydrogen evolution reaction. *J. Am. Chem. Soc.* **135**, 9267–9270 (2013).
25. Izhar, S. & Nagai, M. Transition metal phosphide catalysts for hydrogen oxidation reaction. *Catal. Today* **146**, 172–176 (2009).
26. Yang, X. G. & Wang, C. Y. Nanostructured tungsten carbide catalysts for polymer electrolyte fuel cells. *Appl. Phys. Lett.* **86**, 224104 (2005).
27. Sheng, W. C., Gasteiger, H. A. & Shao-Horn, Y. Hydrogen oxidation and evolution reaction kinetics on platinum: acid vs alkaline electrolytes. *J. Electrochem. Soc.* **157**, B1529–B1536 (2010).
28. Durst, J. et al. New insights into the electrochemical hydrogen oxidation and evolution reaction mechanism. *Energy Environ. Sci.* **7**, 2255–2260 (2014).
29. Biswal, A., Tripathy, B. C., Sanjay, K., Subbaiah, T. & Minakshi, M. Electrolytic manganese dioxide (EMD): a perspective on worldwide production, reserves and its role in electrochemistry. *RSC Adv.* **5**, 58255–58283 (2015).
30. Toupin, M., Brousse, T. & Belanger, D. Charge storage mechanism of MnO<sub>2</sub> electrode used in aqueous electrochemical capacitor. *Chem. Mater.* **16**, 3184–3190 (2004).
31. Sun, M. et al. Controlled synthesis of nanostructured manganese oxide: crystalline evolution and catalytic activities. *Cryst. Eng. Comm.* **15**, 7010–7018 (2013).
32. *Electric Energy Storage Technology Options: A White Paper Primer on Applications, Costs, and Benefits* Electric Power Research Institute Technical Report 1020676 (Electric Power Research Institute, 2010).
33. Roberts, B. P. & Sandberg, C. The role of energy storage in development of smart grids. *Proc. IEEE* **99**, 1139–1144 (2011).

### Acknowledgements

This work was initiated by the support of the Department of Energy, Office of Basic Energy Sciences, Materials Sciences and Engineering Division, under contract DE-AC02-76-SFO0515.

### Author contributions

W.C. and Y.C. conceived the idea. W.C. designed the battery cells and conducted the electrochemical measurements. W.C. conducted SEM and XRD characterization. A.P. performed the simulation. Y.L. conducted TEM characterization. H.W. performed the XPS analysis. G.C. helped with the GC measurements. Y.C. supervised the project. W.C. and Y.C. contributed to writing the manuscript. W.C. and G.L. contributed equally to this work. All authors discussed the results and commented on the manuscript.

### Competing interests

The authors declare no competing interests.

### Additional information

**Supplementary information** is available for this paper at <https://doi.org/10.1038/s41560-018-0147-7>.

**Reprints and permissions information** is available at [www.nature.com/reprints](http://www.nature.com/reprints).

**Correspondence and requests for materials** should be addressed to Y.C.

**Publisher's note:** Springer Nature remains neutral with regard to jurisdictional claims in published maps and institutional affiliations.